Banding in single crystals during plastic deformation

M. Arul Kumar [a] Sivasambu Mahesh [a,b]

[a] *Department of Mechanical Engineering*

[b] *Department of Aerospace Engineering*

Indian Institute of Technology, Kanpur 208016. India.

Abstract

A rigid-plastic rate-independent crystal plasticity model capable of capturing banding in single crystals subjected to homogeneous macroscopic deformation is proposed. This model treats the single crystal as a 'stack of domains'. Individual domains deform homogeneously while maintaining velocity and traction continuity with their neighbors. All the domains collectively accommodate the imposed deformation. The model predicts lattice orientation evolution, slip distribution, strain localization and band orientation in copper single crystals with imposed plane strain deformation. In quantitative agreement with experimental observations reported in the literature, macroscopic shear banding and regular deformation banding are predicted in initially copper and rotated cube oriented single crystals, respectively, while banding is not predicted in initially Goss oriented single crystals. The model does not, however, predict the experimentally observed orientation of smaller scale dislocation boundaries such as dense dislocation walls.

Key words: crystal plasticity, single crystal, macroscopic shear band, regular deformation band, dislocation boundary

1 Introduction

1.1 Banding

Polycrystal models that predict mechanical response and texture evolution during plastic deformation commonly regard each grain of the polycrystal as a homogeneously deforming entity (Taylor, 1938; Lebensohn and Tomé, 1993; Van Houtte et al., 1999; Mahesh, 2009, 2010). However, an enormous body of experimental metallurgical literature indicates that deformation of grains is inhomogeneous. The inhomogeneity of deformation leads to grain subdivision into misoriented domains called bands, which are demarcated by dislocation boundaries. Dislocation boundaries are of two kinds: incidental and geometrically necessary. Incidental dislocation boundaries are comprised of statistically trapped dislocations. Geometrically necessary dislocation boundaries, on the other hand, are necessary for accommodating incompatibility of plastic deformation (Nye, 1953). The volumes delineated by these boundaries are called bands. They are classified based on their size-scale and structure, e.g., Gil Sevillano et al. (1980); Hansen and Juul Jensen (1999). The present work focuses on the formation and evolution of two types of bands, viz., regular deformation bands (RDBs) and macroscopic shear bands (MSBs). The longest dimension of RDBs and MSBs is comparable to the grain size. Smaller scale geometrically necessary dislocation boundaries, which delineate regions whose longest dimension is of the order of tens of dislocation mean free paths, called dense dislocation walls/microbands (DDW-MBs) are also of interest presently.

* Corresponding author
Email address: smahesh@iitk.ac.in (Sivasambu Mahesh).

The constraint experienced by an individual grain in a polycrystal is mediated by the grains surrounding it and generally differs from the macroscopic constraint imposed upon the polycrystal. However, single crystals subjected to plastic deformation experience the imposed macroscopic constraint. This makes single crystals better suited for the study of banding under imposed homogeneous deformation.

1.2 Models of banding

Van Houtte et al. (1979) and Dillamore et al. (1979) proposed that strain localization occurs within MSBs when the effective hardening rate therein becomes negative on account of the local geometrical softening due to lattice rotation being in excess of the local hardening rate of the slip systems. A rigorous analytical methodology embodying this physical notion was given by Asaro (1979), formally based on the considerations of Biot (1965) and Hill and Hutchinson (1975). In this approach, banding was identified with the existence of inhomogeneous solutions of the equations governing the stress-rate fields in the crystal. As the governing equations are not directly solvable, Asaro (1979) considered a reduced problem wherein the inhomogeneity is confined within a rectangular strip, or band, that cuts across the crystal. The inhomogeneous fields that solve the reduced problem are obtained either directly (Asaro, 1979) or by phrasing the problem in variational terms. The latter approach, which also allows for the energetic contribution of band boundaries, has been taken by Kratochvíl et al. (2007).

The analytical approach (Asaro, 1979; Kratochvíl et al., 2007) yields conditions for the onset of banding in closed form at practically no computational

cost for specific lattice orientations. It is ideally suited to lattice orientations wherein only a few slip systems are activated and slip system hardening has a simple form, as in Asaro (1979) and Kratochvíl et al. (2007). This approach becomes highly laborious for lattice orientations undergoing general multi-slip and non-uniform hardening.

Studies based on the crystal plasticity finite element method (CPFEM) have sought to capture the development of grain-level deformation inhomogeneity for grains of arbitrary crystallography undergoing general multi-slip with possibly non-uniform hardening (Pierce et al., 1982; Raabe et al., 2004; Rezvanian et al., 2006; Kuroda and Tvergaard, 2007; Si et al., 2008; Groh et al., 2009; Zhang et al., 2009; Kanjarla et al., 2010). An initial perturbation in model single crystal sample geometry (Pierce et al., 1982; Zhang et al., 2009), local lattice orientation (Raabe et al., 2004), shear imbalance (Rezvanian et al., 2006) or slip system hardness (Kuroda and Tvergaard, 2007) triggers the development of local slip and/or local lattice orientation inhomogeneities. Pierce et al. (1982) predicted a band of higher plastic strain than the matrix and associated it with shear banding observed experimentally. More recently, Rezvanian et al. (2006) and Si et al. (2008) have identified RDBs without intense shear localization in their initially cube oriented simulated aluminum crystals. Under imposed plane strain deformation, they find good agreement between their predicted lattice orientation variation along the normal direction with the experimental observations of Liu and Hansen (1998). Kanjarla et al. (2010) predicted RDB formation in a nearly rotated cube oriented grain in a model columnar polycrystal. They also found the RDB pattern in their model grain to be affected by the inter-granular interactions.

CPFEM simulations, however, come at a high computational cost. Spatial

resolution of the material response in millimeter scale single crystals wherein much of the deformation is confined to shear bands, each only a few microns wide (Wróbel et al., 1994; Wagner et al., 1995), requires a fine mesh (Pierce et al., 1983; Anand and Kalidindi, 1993), higher order elements (Kuroda and Tvergaard, 2007) or the explicit treatment of large strain gradients across shear band boundaries (Anand et al., 2012). Spatial resolution of the deformation field in single crystals undergoing homogeneous deformation or those forming RDBs without intense shear localization is more computationally tractable (Rezvanian et al., 2006; Si et al., 2008; Kanjarla et al., 2010), as a coarser mesh suffices to resolve the smaller strain gradients.

Approaches to predict banding in single crystals that lie in between the computationally light but laborious analytical approach and the computationally intensive but general CPFEM approach are provided by crystal plasticity based models. These are two to three orders of magnitude computationally less intensive than CPFEM and yet sufficiently general to treat arbitrary slip activity and hardening laws. A class of such models capable of predicting the formation of arbitrarily oriented shear bands on the basis of existence of inhomogeneous solutions to the governing equations is due to Needleman and Rice (1978) and Kuroda and Tvergaard (2007). Another class of such models, due to Chin et al. (1969), Lee and Duggan (1993), Lee et al. (1993), Ortiz and Repetto (1999) and Ortiz et al. (2000) is based on experimental observations of patchy slip in grains, whereby deformation by single slip in spatially separate domains is observed in preference to homogeneous multi-slip. The model of Lee and Duggan (1993) and Lee et al. (1993) predicts regular deformation banding by seeking to reduce the work of plastic deformation. The variational theory of Ortiz and Repetto (1999) seeks to minimize a functional that, in

effect, depends on both plastic power and the rate of plastic power. The latter term incorporates the latent hardening. The variational theory predicts banding because the functional can be reduced by lowering latent hardening, which in turn is accomplished by replacing multislip activity in a homogeneously deforming crystal with single slip activity within spatially isolated bands.

Another class of crystal plasticity based models capable of predicting regular deformation banding and macroscopic shear banding has been developed in foregoing works (Mahesh and Tomé, 2004; Mahesh, 2006). In these works, a banded single crystal is represented as a pair of regions that model a pair of compatibly deforming bands. The lattice orientation of both regions are initially identical apart from a small perturbation. The growth of this perturbation with deformation, called orientational instability (Mahesh, 2006), is identified with banding, while its diminution with further deformation, called orientational stability, points to the dominance of a homogeneous deformation mode.

While the aforementioned models and the present model for the inhomogeneous deformation of a single crystal have an energetic basis, a non-energetic reason for banding, viz., Taylor ambiguity, was suggested by Chin and Wonsiewicz (1969) and termed Type 1 banding by Chin (1971). Taylor ambiguity refers to the possibility of accommodating the imposed deformation by activating different set of slip systems in different parts of the single crystal or grain. Leffers (2001a,b) suggested that Taylor ambiguity may underlie the experimentally observed subdivision of grains by DDW-MBs. For two assumed orientations of the band boundaries, he investigated the possible solutions for the slip rates in a pair of compatibly deforming bands caused by Taylor am-

biguity, subject to the constraint that a total of 8 slip systems must activate in both bands to accommodate the imposed plane strain deformation.

1.3 Present work

A model capable of predicting the formation and evolution of MSBs and RDBs during plastic deformation of copper single crystals is presently developed. This model is based on the recently proposed 'stack of domains' model (Arul Kumar et al., 2011). The single crystal is regarded as a one-dimensional stack of domains that collectively accommodate the imposed deformation. The domains deform homogeneously and compatibly with their neighbors. Notable differences with the 'stack of domains' model are: (1) substructure based hardening of domain slip systems, (2) introduction of rules to identify MSB and RDB domains and (3) accounting for mobility of domain boundaries.

The present model is used to simulate plane strain compression of copper single crystals. In agreement with experimental observations reported in the literature, the model predicts the formation of MSBs and RDBs in the initially copper and rotated cube oriented single crystals, respectively, and the formation of neither in the Goss oriented single crystal.

2 Experimental evidence

Relevant facts from the experimental literature about three types of bands, viz., dense dislocation walls-microbands (DDW-MBs), macroscopic shear bands (MSBs) and regular deformation bands (RDBs), are now presented.

2.1 Dense dislocation walls and microbands (DDW-MBs)

Dislocation structures called dense dislocation walls (DDW) and microbands (MBs) that bound regions a few dislocation mean free paths long have been reported in plastically deformed copper. Bay et al. (1989) noted that DDWs and MBs appear together as if forming one general feature, which they called DDW-MBs. These structures, across which the lattice misorientation is of the order of a few degrees, are mobile relative to the crystal material (Albou et al., 2010).

Depending on the lattice orientation and the imposed deformation, DDW-MBs may or may not lie parallel to active slip planes (Hughes and Hansen, 1993; Liu et al., 1998). Winther et al. (1997) have attempted to correlate the formation of crystallographic DDW-MBs with the coplanar slip fraction (CSF), which they defined as the ratio of the largest accumulated slip in a crystallographic slip plane to the total accumulated slip in a grain. They observed experimentally that CSF ≥ 0.45 in about 75% of rolled aluminum grains, which form crystallographic DDW-MBs parallel to the most active crystallographic slip plane and that CSF < 0.45 in about 75% of the experimentally studied grains forming non-crystallographic DDW-MBs. The CSF thus provides a good indicator for the formation of crystallographic DDW-MBs. The CSF indicator, however, misclassifies about 25% of the grains.

2.2 Macroscopic shear bands

Crystallographic DDW-MBs aligned with the dominant crystallographic slip plane act as barriers to slip systems non-coplanar with the dominant crystallo-

graphic slip plane. Non-coplanar slip activity therefore concentrates in regions where the crystallographic DDW-MBs barriers are few or weak and results in severe localized deformation in these regions. The sub-structural elements formed during such localized deformation are the long and narrow microscopic shear bands (Nakayama and Morii, 1982; Duggan et al., 1978). In f.c.c. copper single crystals deformed quasistatically at room temperature, the presence of a single set of pre-existing DDW-MBs parallel to the dominant crystallographic slip plane is a necessary condition for microscopic shear banding (Nakayama and Morii, 1982).

A macroscopic shear band (MSBs) in a single crystal is comprised of a cluster of microscopic shear bands. It typically extends across the crystal and undergoes much more slip than the surrounding material, called the matrix (Duggan et al., 1978; Morii and Nakayama, 1981; Nakayama and Morii, 1982; Hatherly and Malin, 1984; Wagner et al., 1995; Jasienski et al., 1996). The typical misorientation of an MSB with the matrix is of the order of tens of degrees.

Microscopic shear bands, once nucleated, propagate to their final dimensions rapidly and remain inoperative thereafter (Duggan et al., 1978; Hatherly and Malin, 1984; Wagner et al., 1995); nucleation and propagation of new microscopic shear bands elsewhere within the MSB is required to accommodate its subsequent deformation. The direction of propagation of microscopic shear bands evolves gradually during the deformation resulting in apparent mobility of the MSB boundaries (Jasienski et al., 1996). Both microscopic shear band and MSB boundaries do not have simple crystallographic alignments (Wagner et al., 1995; Jasienski et al., 1996).

Various types of dislocation structures have been reported within MSBs in cop-

per single crystals deformed quasistatically at room temperature: microbands parallel to the MSB walls (Wróbel et al., 1994), thin elongated cell structure (Morii and Nakayama, 1981), equiaxed cells (Paul et al., 2010), dynamically recovered cell structure (Wróbel et al., 1996) and no apparent cell structure (Korbel and Szczerba, 1982). Korbel and Szczerba (1982) have suggested that enhanced dynamic recovery (D.R.-2) occurs in the MSB due to the activation of slip systems not coplanar with pre-existing dislocation structures. Blicharski et al. (1995) have suggested that dynamic recovery enhancement in MSBs may be aided by temperature rise, which may accompany rapid local strain accumulation even in thermally conductive copper. Finally, Huang et al. (2006) have reported deformation twinning within shear bands formed in coarse-grained copper at room temperature deformed quasistatically. They have suggested that the high resolved shear stress required for deformation twinning under these conditions is realized within MSBs after substantial hardening of the MSB material.

2.3 Regular deformation bands

A single crystal may divide into lath-shaped regions called regular deformation bands, each several tens of dislocation mean free paths wide and extending across the entire crystal. The deformation and lattice orientation within each region is approximately uniform and distinct from that of its neighbors. Intense shear localization is not normally associated with such regular deformation banding. RDBs have been variously termed type-2 bands (Chin, 1971), deformation bands (Lee et al., 1993), matrix bands (Liu and Hansen, 1998), primary regular deformation bands (Kulkarni et al., 1998; Kuhlmann-

Wilsdorf, 1999) and special bands of secondary slip (Wert et al., 2005).

In f.c.c copper and aluminum, RDBs develop from geometrically necessary dislocation walls, which form along {110} planes perpendicular to the direction of predominant slip (Cahn, 1951; Heye and Sattler, 1971; Cizek et al., 1995). Misorientation between RDBs progressively increases with deformation (Barrett, 1939; Barrett and Levenson, 1940) and may be of the order of tens of degrees (Akef and Driver, 1991; Liu and Hansen, 1998). RDB boundaries also deviate increasingly from the crystallographic {110} plane (Cahn, 1951) with continuing deformation. Regular deformation banding of single crystals typically begins in the early stages of deformation and the number and volume of bands does not change with further deformation (Cahn, 1951; Heye and Sattler, 1971; Lee et al., 1993; Wert et al., 2005). Unlike DDW-MBs and MSBs, RDB boundaries are immobile relative to the material (Wert et al., 2005). Regular deformation banding is observed only in the absence of pre-existing crystallographic DDW-MBs (Wróbel et al., 1994; Liu and Hansen, 1998). However, once formed, slip is predominantly confined to a single slip plane and results in the formation of a set of crystallographic DDW-MBs (Wróbel et al., 1988; Liu and Hansen, 1998).

3 Model

3.1 Standard rate-independent crystal plasticity

Every material point of a single crystal is assumed to follow the standard rigid-plastic rate-independent volume preserving constitutive response (Taylor, 1938; Bishop and Hill, 1951; Kocks et al., 1998). If the slip-rate tensor at

the material point is denoted by $\boldsymbol{L}_{\text{ss}}$,

$$\boldsymbol{L}_{\text{ss}} = \sum_{s=1}^{S} \dot{\gamma}_s \boldsymbol{b}_s \otimes \boldsymbol{n}_s, \tag{1}$$

where $\dot{\gamma}_s$ denotes the slip-rate of slip system $s \in \{1, 2, \ldots, S\}$ and $\boldsymbol{b}_s$ is the Burgers vector or unit slip directional vector of slip system s with slip plane normal $\boldsymbol{n}_s$. $\boldsymbol{b}_s$ and $\boldsymbol{n}_s$ depend upon the lattice orientation of the material point described completely by the orthonormal tensor $\boldsymbol{\Omega}$, which transforms the vectors $\boldsymbol{B}_s$ and $\boldsymbol{N}_s$ that describe the unit slip directional vector and slip plane normal of slip system s in the crystal coordinate system into the $\boldsymbol{b}_s$ and $\boldsymbol{n}_s$ in the reference coordinate system following

$$\boldsymbol{b}_s = \boldsymbol{\Omega}\boldsymbol{B}_s, \quad \text{and} \quad \boldsymbol{n}_s = \boldsymbol{\Omega}\boldsymbol{N}_s. \tag{2}$$

The symmetric part of the slip-rate tensor, $\boldsymbol{L}_{\text{ss}}$, is the strain-rate tensor, $\dot{\boldsymbol{\epsilon}}$,

$$\dot{\boldsymbol{\epsilon}} = (\boldsymbol{L}_{\text{ss}} + \boldsymbol{L}_{\text{ss}}^T)/2 = \sum_{s=1}^{S} \dot{\gamma}_s \boldsymbol{m}_s, \tag{3}$$

where, $\boldsymbol{m}_s$ denotes the Schmid tensor of slip system s

$$\boldsymbol{m}_s = (\boldsymbol{b}_s \otimes \boldsymbol{n}_s + \boldsymbol{n}_s \otimes \boldsymbol{b}_s)/2. \tag{4}$$

If $\boldsymbol{L}$ denotes the velocity gradient at the material point, the lattice spin tensor, $\dot{\boldsymbol{W}}_c$ of the material point, is given by (Kocks et al., 1998)

$$\dot{\boldsymbol{W}}_c = \text{skew}\left(\boldsymbol{L} - \boldsymbol{L}_{\text{ss}}\right). \tag{5}$$

The deformation gradient of a material point, $\boldsymbol{F}$, describes the local shape and evolves following the flow law (Gurtin, 1981),

$$\dot{\boldsymbol{F}} = \boldsymbol{L}\boldsymbol{F}. \tag{6}$$

Let $\boldsymbol{\sigma}$ denote the deviatoric part of the Cauchy stress at the material point. Schmid's law (Kocks et al., 1998) states that slip system s may have non-zero slip-rate only if the resolved shear stress, $\boldsymbol{\sigma} : \boldsymbol{m}_s \equiv \text{tr}(\boldsymbol{\sigma}\boldsymbol{m}_s{}^T)$, equals the critical resolved shear stress (CRSS) on slip system s, τ_s. Thus,

$$\dot{\gamma}_s \begin{cases} \geq 0, & \text{if } \boldsymbol{\sigma} : \boldsymbol{m}_s = \tau_s, \\ = 0, & \text{if } \boldsymbol{\sigma} : \boldsymbol{m}_s < \tau_s. \end{cases} \tag{7}$$

Taylor's principle (Taylor, 1938) asserts that for given $\dot{\boldsymbol{\epsilon}}$ of all possible slip-rate combinations $\{\dot{\gamma}_s, s \in \{1, \ldots, S\}\}$ that respect the constraint given by Eq. (3), those which minimize the plastic power of deformation

$$P = \sum_{s=1}^{S} \tau_s \dot{\gamma}_s \tag{8}$$

are preferred. Chin and Mammel (1969) have shown that the set of slip-rates, $\dot{\gamma}_s$, which minimize P subject to the constraint given by Eq. (3) automatically satisfies Eq. (7). $\{\dot{\gamma}_s, s \in \{1, \ldots, S\}\}$ that minimizes P given by Eq. (8) subject to the constraint Eq. (3) may be non-unique. In this case, the consistency condition and algorithm for its implementation given by Anand and Kothari (1996) is invoked to ensure that $\dot{\gamma}_s > 0$ in the largest number of slip systems.

Slip systems harden with deformation. The evolution of the critical resolved shear stress of the s-th slip system is taken to follow (Hill, 1966; Kocks et al., 1998)

$$\dot{\tau}_s = \frac{d\tau}{d\Gamma} \sum_{s'=1}^{S} H_{ss'} \dot{\gamma}_{s'}, \tag{9}$$

where $[H]$ is the latent hardening matrix,

$$\Gamma = \sum_{s=1}^{S} \gamma_s, \tag{10}$$

is the total accumulated slip at the material point and γ_s is the accumulated slip in the s-th slip system. In the present work, τ is taken to follow the extended Voce law given by Tomé et al. (1984),

$$\tau(\Gamma) = \tau_0 + (\tau_1 + \theta_1\Gamma)[1 - \exp(-\Gamma\theta_0/\tau_1)], \tag{11}$$

where τ_0, τ_1, θ_0 and θ_1 are material hardening parameters.

3.2 The 'stack of domains' model of a single crystal

3.2.1 Geometry

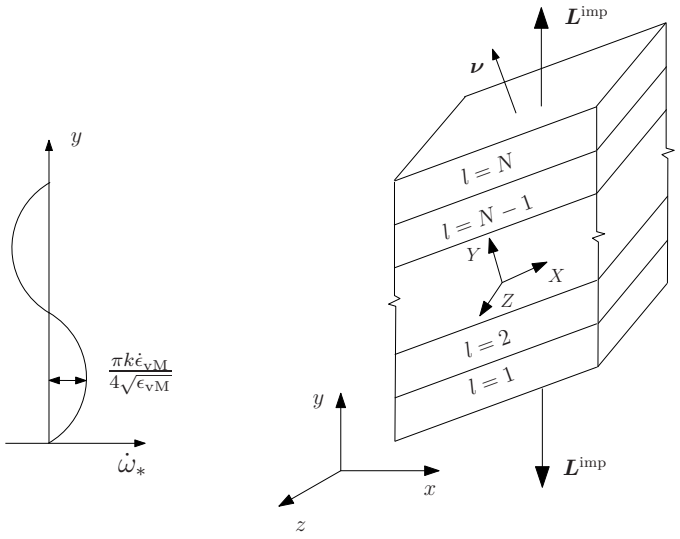

Fig. 1. A single crystal modeled as a stack of N parallelepiped-shaped domains. XYZ is a domain boundary fixed coordinate system; $\boldsymbol{\nu} \parallel Y$ denotes the domain boundary normal. The sinusoidal lattice orientation perturbation rate of individual domains is also schematically represented.

A model of a rigid-plastic rate-independent single crystal capable of representing banding is presently described. The single crystal, shown schematically in Fig. 1, is represented as a stack of N parallelepiped-shaped domains each of which is endowed with a uniform lattice orientation and is assumed to deform

homogeneously. A single domain or a group of neighboring domains may represent a deformation band. The geometric shapes of the individual domains are assumed to be identical, so that the volume fraction $\rho^{[l]}$ of the l-th domain is simply $\rho^{[l]} = 1/N$, for $l = 1, 2, \ldots, N$. Stacking is assumed to be repeated periodically so that neighbors of domain l in the stack are $(l + 1 \bmod N)$ and $(l - 1 \bmod N)$. Domain boundaries between adjacent parallelepiped-shaped domains are assumed to be planar and identically oriented. For convenience, the domain boundary between domains $(l \bmod N)$ and $(l + 1 \bmod N)$ is numbered as the l-th domain boundary. Quantities with superscripts enclosed in square brackets, e.g., $\{\cdot\}^{[l]}$, are associated with domain l while, quantities with superscripts enclosed in parentheses, e.g., $\{\cdot\}^{(l)}$, are associated with domain boundary l.

All the domain boundaries in the 'stack of domains' model are assumed to be oriented identically with normal $\boldsymbol{\nu}$, as shown in Fig. 1. This is reasonable, since only the boundaries enclosing domains representing MSBs or RDBs, which are experimentally observed (Sec. 2) to be delineated by approximately parallel boundaries, are physically significant. This assumption implies that only one set of deformation bands can be predicted by the present model even in crystals wherein deformation bands at different length scales simultaneously form. Moreover, the predicted deformation bands will necessarily be the largest bands in the single crystal under consideration. Two sets of cartesian coordinates: the sample coordinate system xyz and a domain boundary fixed coordinate system XYZ with the Y-axis always aligned with the normal vector $\boldsymbol{\nu}$ are also shown.

The present geometric arrangement of domains within a single crystal is similar to the geometric arrangement of grains within a polycrystalline sub-aggregate

studied by Arul Kumar et al. (2011).

3.2.2 Lattice orientation perturbation

If the lattice orientation in all the domains comprising the stack were identical, the 'stack of domains' model would represent a perfect single crystal. In this case, each domain would undergo the same deformation as the single crystal, i.e., single crystal would deform homogeneously. However, even in an initially perfect single crystal, lattice orientation perturbations arise during plastic deformation. Across incidental dislocation boundaries, for instance, Hughes et al. (1997, 1998) have observed that the average absolute misorientation angle $\langle|\omega_*|\rangle$ scales with von Mises strain ϵ_{vM} as

$$\langle|\omega_*|\rangle = k\epsilon_{\mathrm{vM}}^{1/2}. \tag{12}$$

The misorientation rate follows from Eq. (12), and is given by,

$$\langle|\dot{\omega}_*|\rangle = \frac{k\dot{\epsilon}_{\mathrm{vM}}}{2\sqrt{\epsilon_{\mathrm{vM}}}}, \tag{13}$$

where, the von Mises strain-rate, $\dot{\epsilon}_{\mathrm{vM}}$, is given by

$$\dot{\epsilon}_{\mathrm{vM}} = \sqrt{\frac{2}{3}\mathrm{tr}\ (\dot{\boldsymbol{\epsilon}}^2)}. \tag{14}$$

Following Eq. (13), the lattice rotation rate in the l-th domain is prescribed as

$$\dot{\omega}_*^{[l]} = \frac{\pi k\dot{\epsilon}_{\mathrm{vM}}}{4\sqrt{\epsilon_{\mathrm{vM}}}}\sin\left(\frac{2\pi l}{N}\right), \tag{15}$$

as schematized in Fig. 1. This lattice rotation is about a unit misorientation vector, $\hat{\boldsymbol{m}}$, uniformly distributed on the unit sphere. The tensorial lattice spin

of the l-th domain caused by the lattice orientation perturbation is thus

$$\dot{\boldsymbol{W}}_*^{[l]} = \dot{\omega}_*^{[l]}(\hat{\boldsymbol{m}}\times), \tag{16}$$

where, $\hat{\boldsymbol{m}}\times$ denotes the skew-symmetric tensor whose axial is the vector $\hat{\boldsymbol{m}}$.

It turns out that the state evolution of the 'stack of domains' model is not sensitive to the functional form assumed in Eq. (15). Even if the $\dot{\omega}_*^{[l]}$ were drawn from a uniform distribution of mean $\langle|\dot{\omega}_*|\rangle$ given by Eq. (13), the predictions of the present model, given in Sec. 4, remain practically unchanged. The role of the lattice orientation perturbation is simply to trigger the initial slip inhomogeneity amongst domains in the numerical calculation.

3.2.3 Kinematics

Let $\bar{\boldsymbol{L}}$ denote the macroscopic velocity gradient of the 'stack of domains' representing the model single crystal. $\bar{\boldsymbol{L}}$ is taken to be the volume fraction weighted average of the velocity gradients, $\boldsymbol{L}^{[l]}$, of individual domains, l, i.e.,

$$\sum_{l=1}^{N} \rho^{[l]} \boldsymbol{L}^{[l]} = \bar{\boldsymbol{L}}. \tag{17}$$

The shape of the model single crystal represented by stack of domains is described by deformation gradient, $\bar{\boldsymbol{F}}$. The flow law, which determines the evolution of $\bar{\boldsymbol{F}}$ parallels Eq. (6) and is

$$\dot{\bar{\boldsymbol{F}}} = \bar{\boldsymbol{L}}\bar{\boldsymbol{F}}. \tag{18}$$

3.2.4 Boundary and continuity conditions

Let $\boldsymbol{L}^{\text{imp}}$ be the velocity gradient imposed upon the single crystal that must be collectively accommodated by its domains, i.e.,

$$\bar{\boldsymbol{L}} = \boldsymbol{L}^{\text{imp}}. \tag{19}$$

Let $\dot{\boldsymbol{\epsilon}}^{\text{imp}} = (\boldsymbol{L}^{\text{imp}} + \boldsymbol{L}^{\text{imp}^T})/2$ be the imposed strain-rate on the single crystal. It then follows from Eqs. (3), (5), (17) and (19) that

$$\sum_{l=1}^{N} \rho^{[l]} \dot{\boldsymbol{\epsilon}}^{[l]} = \dot{\boldsymbol{\epsilon}}^{\text{imp}}. \tag{20}$$

Let $p^{[l]}$ denote the scalar hydrostatic pressure in domain l so that the Cauchy stress therein is $p^{[l]}\boldsymbol{I} + \boldsymbol{\sigma}^{[l]}$. Traction continuity conditions between neighboring domains in the model in the XYZ coordinate system are then:

$$\begin{aligned} \sigma_{\text{XY}}^{[l \bmod N]} &= \sigma_{\text{XY}}^{[l+1 \bmod N]}, \\ \sigma_{\text{YZ}}^{[l \bmod N]} &= \sigma_{\text{YZ}}^{[l+1 \bmod N]}, \\ p^{[l \bmod N]} + \sigma_{\text{YY}}^{[l \bmod N]} &= p^{[l+1 \bmod N]} + \sigma_{\text{YY}}^{[l+1 \bmod N]}. \end{aligned} \tag{21}$$

It is not required to enforce the third equation of Eq. (21) explicitly because its satisfaction is automatic: It can be shown (Arul Kumar et al., 2011) that the third equation of Eq. (21) can always be satisfied for arbitrary $\{\sigma_{\text{YY}}^{[l]} : l \in \{1, 2, \ldots, N\}\}$ by suitable choice of the domain hydrostatic pressure components $\{p^{[l]} : l \in \{1, 2, \ldots, N\}\}$. Moreover, $p^{[l]}$ does not affect the rigid-plastic volume-preserving deformation of the domains.

Traction continuity and compatibility conditions between neighboring domains that must be explicitly enforced in the model are thus (Arul Kumar et al., 2011):

$$
\begin{aligned}
\sigma_{\mathrm{XY}}^{[l \bmod N]} &= \sigma_{\mathrm{XY}}^{[l+1 \bmod N]}, \\
\sigma_{\mathrm{YZ}}^{[l \bmod N]} &= \sigma_{\mathrm{YZ}}^{[l+1 \bmod N]}, \\
\dot{\epsilon}_{\mathrm{XX}}^{[l \bmod N]} &= \dot{\epsilon}_{\mathrm{XX}}^{[l+1 \bmod N]}, \\
\dot{\epsilon}_{\mathrm{ZZ}}^{[l \bmod N]} &= \dot{\epsilon}_{\mathrm{ZZ}}^{[l+1 \bmod N]}, \text{ and} \\
\dot{\epsilon}_{\mathrm{XZ}}^{[l \bmod N]} &= \dot{\epsilon}_{\mathrm{XZ}}^{[l+1 \bmod N]},
\end{aligned}
\tag{22}
$$

for $l \in \{1, 2, \ldots, N\}$.

Following Hill (1961), the velocity continuity condition between domains l and $l+1$ can be written as

$$
[\![\boldsymbol{L}^{(l)}]\!] = \boldsymbol{L}^{[l+1 \bmod N]} - \boldsymbol{L}^{[l \bmod N]} = \boldsymbol{\lambda}^{(l)} \otimes \boldsymbol{\nu}, \tag{23}
$$

where $\boldsymbol{\lambda}^{(l)}$, Hadamard's characteristic segment of domain boundary l, is given by (Mahesh, 2006)

$$
\boldsymbol{\lambda}^{(l)} = 2[\![\dot{\boldsymbol{\epsilon}}^{(l)}]\!]\boldsymbol{\nu} + ([\![\dot{\boldsymbol{\epsilon}}^{(l)}]\!]\boldsymbol{\nu} \cdot \boldsymbol{\nu})\boldsymbol{\nu}. \tag{24}
$$

Eq. (19) may be written using Eq. (5) as

$$
\sum_{l=1}^{N} \rho^{[l]} \left(\boldsymbol{L}_{\mathrm{ss}}^{[l]} + \dot{\boldsymbol{W}}_{c}^{[l]} \right) = \boldsymbol{L}^{\mathrm{imp}}. \tag{25}
$$

Algebraic manipulation detailed in Arul Kumar et al. (2011) of Eqs. (23) and (25) using Eqs. (24) and (5) yields

$$
\dot{\boldsymbol{W}}_{c}^{[l]} = \mathrm{skew} \left(\boldsymbol{L}^{\mathrm{imp}} - \boldsymbol{L}_{ss}^{[l]} + \boldsymbol{\Phi}^{[l]} - \boldsymbol{\Phi}^{\mathrm{imp}} \right), \tag{26}
$$

where,

$$
\begin{aligned}
\boldsymbol{\Phi}^{[l]} &= \left[2\dot{\boldsymbol{\epsilon}}^{[l]}\boldsymbol{\nu} - (\dot{\boldsymbol{\epsilon}}^{[l]}\boldsymbol{\nu} \cdot \boldsymbol{\nu})\boldsymbol{\nu} \right] \otimes \boldsymbol{\nu} \text{ and} \\
\boldsymbol{\Phi}^{\mathrm{imp}} &= \left[2\dot{\boldsymbol{\epsilon}}^{\mathrm{imp}}\boldsymbol{\nu} - (\dot{\boldsymbol{\epsilon}}^{\mathrm{imp}}\boldsymbol{\nu} \cdot \boldsymbol{\nu})\boldsymbol{\nu} \right] \otimes \boldsymbol{\nu}.
\end{aligned}
\tag{27}
$$

By comparing Eqs. (26) and (5) it is seen that the lattice spin of domain l in the 'stack of domains' model subjected to imposed velocity gradient $\boldsymbol{L}^{\text{imp}}$ differs from that of a material point subjected to the same velocity gradient by skew$(\boldsymbol{\Phi}^{[l]} - \boldsymbol{\Phi}^{\text{imp}})$. It also follows from Eq. (27) that $\sum_{l=1}^{N} \rho^{[l]}$ skew$(\boldsymbol{\Phi}^{[l]} - \boldsymbol{\Phi}^{\text{imp}}) = \boldsymbol{0}$. Therefore, skew$(\boldsymbol{\Phi}^{[l]} - \boldsymbol{\Phi}^{\text{imp}})$ represents the local deviation of the lattice spin of domain l from that of the average (Kocks et al., 1998, § 11.4.2). Parallel to Eq. (24), this deviation can be written as

$$\text{skew}(\boldsymbol{\Phi}^{[l]} - \boldsymbol{\Phi}^{\text{imp}}) = \boldsymbol{\Lambda}^{[l]} \otimes \boldsymbol{\nu}, \tag{28}$$

where, $\boldsymbol{\Lambda}^{[l]} = 2(\dot{\boldsymbol{\epsilon}}^{[l]} - \dot{\boldsymbol{\epsilon}}^{\text{imp}})\boldsymbol{\nu} + ((\dot{\boldsymbol{\epsilon}}^{[l]} - \dot{\boldsymbol{\epsilon}}^{\text{imp}})\boldsymbol{\nu} \cdot \boldsymbol{\nu})\boldsymbol{\nu}$ denotes the Hadamard characteristic segment between two material points deforming with strain-rates $\dot{\boldsymbol{\epsilon}}^{[l]}$ and $\dot{\boldsymbol{\epsilon}}^{\text{imp}}$ compatibly across an interface oriented normal to $\boldsymbol{\nu}$.

The net lattice spin in the l-th domain is simply the sum of the lattice spins imposed by the lattice orientation perturbation and by the requirement for compatibility across domain interfaces. Thus,

$$\dot{\boldsymbol{W}}^{[l]} = \dot{\boldsymbol{W}}_{*}^{[l]} + \dot{\boldsymbol{W}}_{c}^{[l]}, \tag{29}$$

where, the individual terms on the right side are given by Eqs. (16) and (26). An algorithm to solve for the slip rates, $\dot{\gamma}_s$, in all the domains subject to the conditions imposed by Eqs. (7), (20) and (22), and consistency conditions (Havner, 1992) has been developed previously (Arul Kumar et al., 2011).

3.3 Orientational stability

The notion of orientational stability proposed by Mahesh (2006) is now extended to the 'stack of domains' model. Let $\boldsymbol{\Omega}^{[l \bmod N]}$ and $\boldsymbol{\Omega}^{[l+1 \bmod N]}$ be the

orthonormal lattice orientation tensor of the domains l mod N and l+1 mod N separated by domain boundary l that transform vectors from the crystal coordinate system to the sample coordinate system following Eq. (2). Then the misorientation vector between these domains is given by (Kocks et al., 1998)

$$\hat{\boldsymbol{m}}^{(l)} = \text{axial } (\text{skew } (\boldsymbol{\Omega}^{[l \bmod N]} \boldsymbol{\Omega}^{[l+1 \bmod N]^T})). \tag{30}$$

The axial vector of the rate of misorientation between these neighboring domains is

$$\hat{\boldsymbol{w}}^{(l)} = \text{axial } \{\dot{\boldsymbol{W}}^{[l \bmod N]} - \dot{\boldsymbol{W}}^{[l+1 \bmod N]}\}, \tag{31}$$

where $\dot{\boldsymbol{W}}^{[l \bmod N]}$ and $\dot{\boldsymbol{W}}^{[l+1 \bmod N]}$ denote the lattice spin rates of domains l mod N and $l+1$ mod N given by Eq. (26). The domain boundary l between domains l mod N and $l+1$ mod N is said to be orientationally unstable if

$$\mu^{(l)} = \hat{\boldsymbol{m}}^{(l)} \cdot \hat{\boldsymbol{w}}^{(l)} > 0, \tag{32}$$

and orientationally stable otherwise.

Domain boundaries that remain orientationally stable throughout the deformation separate domains of negligible misorientation. They, therefore, do not correspond to physical geometrically necessary dislocation boundaries. On the other hand, domain boundaries that are orientationally unstable, during part or whole of the deformation process may separate misoriented domains and may represent geometrically necessary physical deformation band boundaries. Also, because of the periodicity in the stacking of domains, assumed in Sec. 3.2.1, exactly one domain boundary cannot be orientationally unstable; the number of orientationally unstable domain boundaries can only be zero, two or more.

3.4 Sub-structure

3.4.1 Slip system dominance

As noted in Secs. 2.2 and 2.3, the presence of crystallographic DDW-MBs is a pre-requisite for macroscopic shear banding, while the absence of crystallographic DDW-MBs is necessary for regular deformation banding. Substructure is not directly represented in the present model; DDW-MBs are not explicitly evolved in the course of the simulated deformation of the 'stack of domains' model. The presence or absence of crystallographic DDW-MBs in a domain is inferred from the dominance or non-dominance of slip activity of a single crystallographic slip plane in that domain, respectively.

A quantitative criterion for the formation of crystallographic DDW-MBs based on slip activity in crystallographic slip planes, suggested by Winther et al. (1997), has been discussed in Sec. 2.1. This criterion is unable to discriminate between crystallographic and non-crystallographic DDW-MBs for about 25% of the grains studied by Winther et al. (1997). Another measure of slip concentration in a crystallographic slip plane, which accounts for simultaneously activated cross-slip systems is, therefore, presently suggested. Two slip systems s and t are said to be simultaneously activated cross-slip systems if $\dot{\gamma}_s > 0$, $\dot{\gamma}_t > 0$, $\boldsymbol{b}_s = \boldsymbol{b}_t$ and $\boldsymbol{n}_s \neq \pm\boldsymbol{n}_t$. Screw dislocations gliding in one of a pair of simultaneously activated cross-slip systems may readily cross-slip into the other. They are therefore unlikely to get trapped in their original glide plane. Let $\mathscr{S}^p$ denote the set of slip systems in the crystallographic slip plane p with normal $\boldsymbol{n}^p$, whose cross-slip systems are not simultaneously activated.

Thus,

$$\mathscr{S}^p = \{s : \boldsymbol{n}_s = \pm\boldsymbol{n}^p, \dot{\gamma}_s\dot{\gamma}_t = 0 \text{ if } \boldsymbol{b}_s = \boldsymbol{b}_t \text{ and } \boldsymbol{n}_s \neq \pm\boldsymbol{n}_t\} \tag{33}$$

denotes the set of slip systems that may contribute dislocations to DDW-MBs aligned parallel to the plane p. Even though the mechanism of cross-slip only applies to the screw component of gliding dislocations, for simplicity, both screw and edge dislocation contributions from simultaneously activated cross-slip systems are neglected in Eq. (33).

The effective total slip activity, $\dot{\Gamma}_p$, contributing to DDW-MB formation in the crystallographic slip plane p is then

$$\dot{\Gamma}_p = \sum_{s\in\mathscr{S}^p} |\dot{\gamma}_s|. \tag{34}$$

Let $\dot{\Gamma}_{p^*}$ and $\dot{\Gamma}_{p^{**}}$ be the total slip rates of the most active and second most active crystallographic slip planes, p^* and p^{**}, respectively. The criterion for dominance of the crystallographic slip plane p^*, which is also taken to be the criterion for the formation of DDW-MBs parallel to p^* in pure copper is (Mahesh, 2006)

$$\frac{\dot{\Gamma}_{p^*}}{\dot{\Gamma}_{p^{**}}} \geq 1.2. \tag{35}$$

3.4.2 Sub-structure based hardening

A sub-structure comprised of dislocation cells or non-crystallographic DDW-MBs is referred to as type (i) and a sub-structure comprised of crystallographic DDW-MBs as type (ii). Non-satisfaction and satisfaction of Eq. (35) in a domain of a model copper single crystal are taken to imply the formation of type (i) and type (ii) sub-structures therein, respectively. It has been noted in Sec. 2.2 that crystallographic DDW-MBs interrupted by microscopic shear

bands is one type of sub-structure observed within MSBs. This is termed the type (iii) sub-structure. Type (ii) and type (iii) sub-structures are schematically shown in Figs. 2(a) and (b), respectively. Plastic anisotropy is accounted for by assigning different hardening matrices, $[H^{(\mathrm{i})}]$, $[H^{(\mathrm{ii})}]$ and $[H^{(\mathrm{iii})}]$ in Eq. (9) to each of the three sub-structure types.

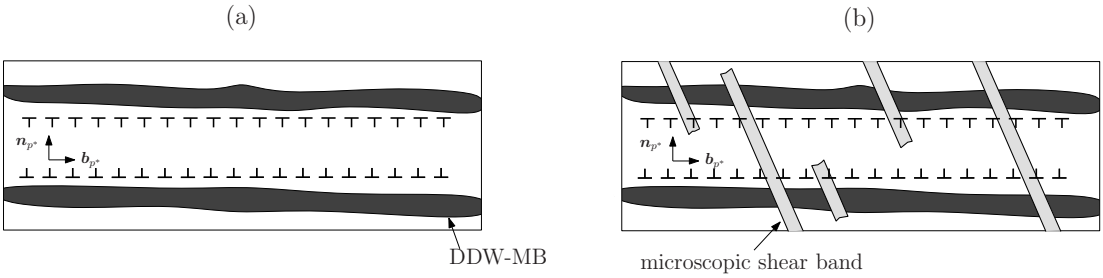

Fig. 2. Schematic representation of (a) type (ii) and (b) type (iii) sub-structures.

In a domain with type (i) sub-structure, plastic anisotropy is assumed negligible, i.e., all slip systems are assumed to harden equally. Thus,

$$H^{(\mathrm{i})}_{ss'} = 1, \quad s, s' \in \{1, 2, \ldots, S\}. \tag{36}$$

In a domain with type (ii) sub-structure, shown in Fig. 2 (a), DDW-MBs parallel to plane p^* act as directional barriers to slip and cause anisotropy in the domain's plastic response. In such domains, the CRSS of slip systems intersecting p^* will exceed that of slip systems parallel to p^*. To reflect this, the elements of the hardening matrix, $[H^{(\mathrm{ii})}]$ are taken as

$$H^{(\mathrm{ii})}_{ss'} = \begin{cases} \alpha \geq 1, & \text{if } \boldsymbol{n}_s \neq \pm\boldsymbol{n}_{p^*},\ \boldsymbol{n}_{s'} = \pm\boldsymbol{n}_{p^*} \text{ and } s \neq s', \\ 1, & \text{otherwise.} \end{cases} \tag{37}$$

As noted in Sec. 2.2, enhanced dynamic recovery and/or deformation twinning may occur within MSBs. This may reduce the hardening rate of slip systems and alter the plastic anisotropy in the MSB material. Neglecting the latter

effect for simplicity, it is presently assumed that the hardening rate $[H^{(\mathrm{iii})}]$ in an MSB domain is proportional to $[H^{(\mathrm{ii})}]$:

$$H^{(\mathrm{iii})}_{ss'} = \chi H^{(\mathrm{ii})}_{ss'}, \quad s, s' \in \{1, 2, \ldots, S\}, \tag{38}$$

where, $0 \leq \chi \leq 1$ indicates a reduced hardening rate in MSB domains. It is emphasized that Eq. (38) does not imply softening of the MSB domain; only a reduction in the hardening rate is proposed. Also, the reduced hardening rate given by Eq. (38) is applied only after MSB nucleation; it is not therefore responsible for MSB nucleation. Finally, it is assumed in Eq. (38) that the mechanisms responsible for reduced hardening of MSB material become active immediately upon MSB nucleation; in reality, these may only be activated after substantial MSB deformation.

3.5 Identification of banding

A contiguous set of domains $\mathscr{D} = \{l, l+1, \ldots, m\}$ is taken to represent a band if their slip pattern and lattice rotations are similar, but differ from that in other domains, denoted $\mathscr{D}^c$. A robust and reliable indication of divergence of the slip pattern and lattice rotations of $\mathscr{D}$ from that of $\mathscr{D}^c$ is provided by orientational instability of the two domain boundaries separating $\mathscr{D}$ from $\mathscr{D}^c$, i.e., $\mu^{(l-1)} > 0$ and $\mu^{(m)} > 0$. Orientationally unstable domain boundaries thus represent band boundaries and the set of domains contained between a pair of nearest orientationally unstable domain boundaries represent a band.

The decision tree followed to identify a set of contiguous domains $\mathscr{D}$ as a particular type of band is shown in Fig. 3. Domains identified as constituents of a band are assumed to remain so during subsequent deformation.

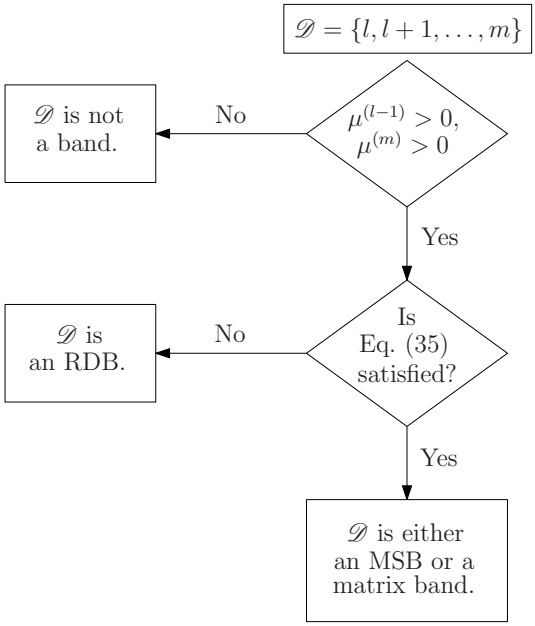

Fig. 3. Flow chart detailing the identification of a set of contiguous domains, $\mathscr{D} = \{l, l+1, \ldots, m\}$, as a particular type of band. The domains comprising $\mathscr{D}$ are not part of a pre-existing band.

3.6 Domain boundary orientation

In order to capture the experimentally observed mobility of band boundaries noted in Secs. 2.1 and 2.2, domain boundaries are assumed be mobile relative to the crystal material. Following Mahesh (2006), their orientation $\boldsymbol{\nu}$ is taken to be that which minimizes the plastic power of the model crystal, i.e.,

$$\boldsymbol{\nu} = \underset{\boldsymbol{\nu}^*}{\operatorname{argmin}} \sum_{l=1}^{N} \rho^{[l]} \sum_{s=1}^{S} \tau_s^{[l]} \dot{\gamma}_s^{[l]}(\boldsymbol{\nu}^*), \tag{39}$$

subject to the constraints given by Eqs. (3), (20) and (22). Since the objective function in Eq. (39) is non-smooth, a section search method (Chang, 2009) is employed for minimization over the unit hemispherical surface spanned by $\boldsymbol{\nu}^*$. Predicted domain boundaries need not coincide with {111} planes.

It was noted in Sec. 2.3 that RDB boundaries are not mobile relative to the

crystal material and therefore, evolve in conformity with the shape of the crystal. Eq. (39) therefore, is not applied to model crystals containing RDB bands. Instead, if $\boldsymbol{\nu_0}$ is the domain boundary normal and $\bar{\boldsymbol{F}}_0$ the deformation gradient at the instant of RDB formation, the domain boundary orientation $\boldsymbol{\nu}$ when the crystal deformation gradient becomes $\bar{\boldsymbol{F}}$ is (Gurtin, 1981)

$$\boldsymbol{\nu} = \frac{\bar{\boldsymbol{F}}_0^{\,T} \bar{\boldsymbol{F}}^{-T} \boldsymbol{\nu}_0}{\|\bar{\boldsymbol{F}}_0^{\,T} \bar{\boldsymbol{F}}^{-T} \boldsymbol{\nu}_0\|}. \tag{40}$$

In crystal orientations forming RDBs, Eq. (39) applies until the instant of banding and Eq. (40) thereafter. $\boldsymbol{\nu_0}$ is, therefore, given by Eq. (39).

4 Results

4.1 Initial lattice orientation

The banding response of copper single crystals subjected to plane strain compression in the plane containing the rolling direction (RD) and the normal direction (ND) is studied. The specimen dimension along the transverse direction (TD) is maintained constant. Three experimentally well-studied crystal orientations are analyzed: copper: ND/RD= $(112)/[11\bar{1}]$ (Bunge angles: $(\phi_1, \varphi, \phi_2) = (-90°, 35.26°, 45°)$), rotated cube: ND/RD= (001)/[110]: (Bunge angles: $(\phi_1, \varphi, \phi_2) = (90°, 0°, -135°)$) and Goss ND/RD= (110)[001] (Bunge angles: $(\phi_1, \varphi, \phi_2) = (90°, 90°, 45°)$). For brevity, these will henceforth be referred to as the C crystal, the RC crystal and the G crystal.

Figs. 4 (a_1), (b_1) and (c_1) show the initial orientation of these crystals together with the four $\{111\}\langle 110\rangle$ slip systems activated during full constraints plane strain compression, following the Schmid-Boas notation (Ortiz and Repetto,

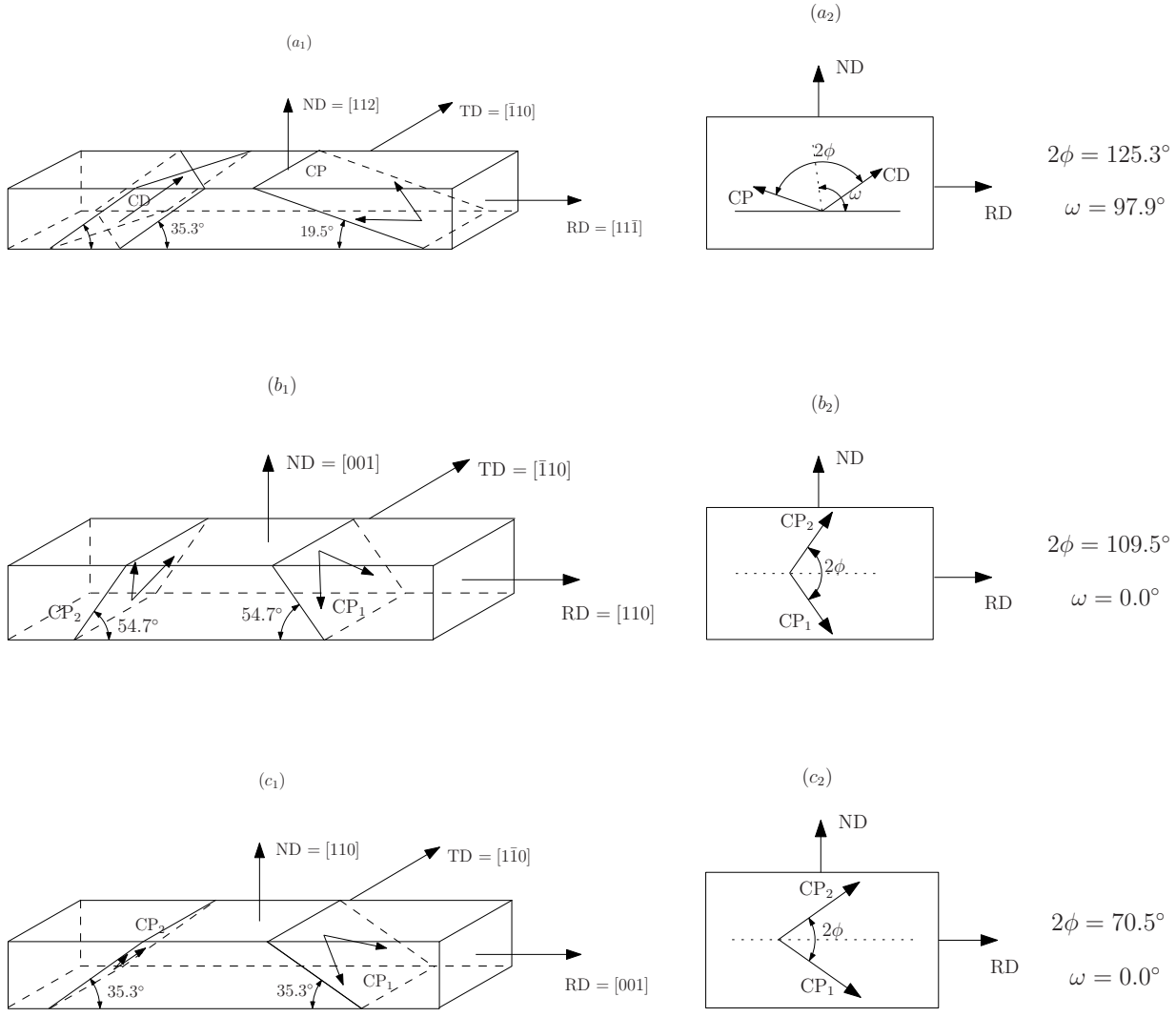

Fig. 4. Crystallography of the three initial lattice orientations of present interest: (a_1) copper (C), (b_1) rotated cube (RC) and (c_1) Goss (G), and their respective, equivalent 2D representations, (a_2), (b_2) and (c_2).

1999). In the C crystal, potential slip activity is divided between two coplanar (CP: $b_2 = (111)[0\bar{1}1]$ and $b_4 = (111)[\bar{1}01]$) and two co-directional slip systems (CD: $a_6 = (\bar{1}11)[110]$ and $d_6 = (1\bar{1}1)[110]$). The RC crystal can potentially activate slip on two pairs of coplanar slip systems (CP_1: $b_2 = (111)[0\bar{1}1]$ and $b_4 = (111)[\bar{1}01]$; CP_2: $c_1 = (\bar{1}\bar{1}1)[011]$ and $c_3 = (\bar{1}\bar{1}1)[101]$). Likewise, in the G crystal two pairs of coplanar slip systems (CP_1: $b_2 = (111)[0\bar{1}1]$ and $b_4 = (111)[\bar{1}01]$; CP_2: $c_1 = (\bar{1}\bar{1}1)[011]$ and $c_3 = (\bar{1}\bar{1}1)[101]$) are activated.

It is evident from Fig. 4 that all three crystals considered are crystallographically symmetric about the RD–ND plane. In view of the symmetry of the imposed plane strain deformation also about the TD, two dimensional analyses of these orientations with two slip systems each, as shown in Figs. 4 (a_2), (b_2) and (c_2), will suffice. Crystal symmetry about the RD–ND plane also ensures that all lattice rotations occur about TD. Thus, a scalar ω, related to the second Bunge angle φ through

$$\omega = \begin{cases} \varphi + 62.64^\circ, & \text{for the C crystal,} \\ \varphi, & \text{for the RC crystal and} \\ \varphi - 90^\circ, & \text{for the G crystal,} \end{cases} \tag{41}$$

and representing the inclination of the angle bisector of the projection of the two slip directions onto the RD–ND plane, together with the included angle 2ϕ between these projections, suffices to represent the lattice orientations of the two-dimensional crystals (Figs. 4 (a_2), (b_2) and (c_2)).

A two-dimensional 'stack of domains' model of a single crystal, which accommodates the plastic slip and lattice rotation within the RD-ND plane is shown in Fig. 5. The sample coordinate system, xy, coincides with the RD-ND system. The domain boundary coordinate system, XY, with Y-axis always normal to the domain boundaries, is confined to the RD-ND plane. A scalar θ, also shown, specifies the domain boundary orientation relative to the xy-system. Plane strain deformation under fully constrained imposed velocity gradient

$$[\boldsymbol{L}]_{\mathrm{RD-ND}} = \begin{bmatrix} 1 & 0 \\ 0 & -1 \end{bmatrix} \tag{42}$$

in the [RD-ND] system is simulated following the procedure detailed in Sec. 3.

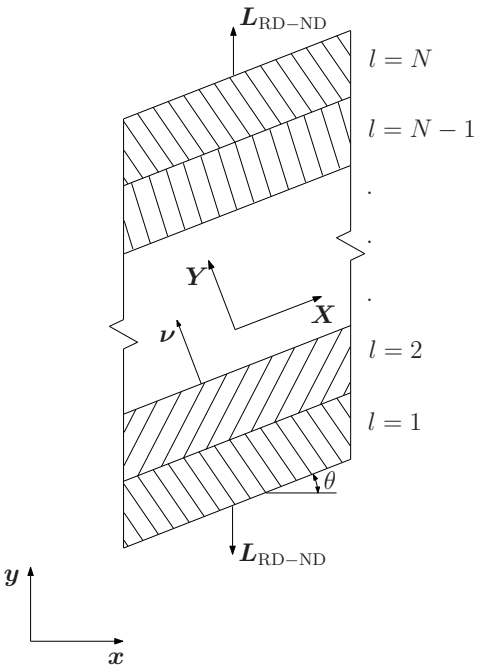

Fig. 5. The two-dimensional 'stack of domains' model comprised of N domains. XY, xy and θ are described in the text.

The single crystal is discretized into a stack of $N = 16$ domains.

4.2 Hardening parameters

Three sets of hardening parameters, τ_0, θ_0, τ_1 and θ_1 (Eq. (11)) were obtained by Tomé et al. (1984) by fitting experimental stress-strain curves for uniaxial tension, compression and torsion in polycrystalline OHFC copper. The response predicted by the present simulations using all three parameter sets are qualitatively similar. Therefore, in the following, predictions corresponding to only one of the parameter sets of Tomé et al. (1984): $\tau_0 = 12$ MPa, $\theta_0 = 160$ MPa, $\tau_1 = 98$ MPa and $\theta_1 = 7$ MPa, is discussed. The hardening matrices corresponding to type (i), type (ii) and type (iii) sub-structures, discussed in

Sec. 3.4.2, are taken to be

$$[H^{(\mathrm{i})}] = \begin{pmatrix} 1 & 1 & \\ & & \\ 1 & 1 & \end{pmatrix}, \quad [H^{(\mathrm{ii})}] = \begin{pmatrix} 1 & \alpha & \\ & & \\ \alpha & 1 & \end{pmatrix} \text{ and } [H^{(\mathrm{iii})}] = \chi \begin{pmatrix} 1 & \alpha & \\ & & \\ \alpha & 1 & \end{pmatrix}, \tag{43}$$

respectively, where, $\alpha = 3.1$ and $\chi = 0.5$. These numbers represent limiting values for these parameters in that for $\alpha < 3.1$ or $\chi > 0.5$, macroscopic shear banding in the C crystal, reported below, is not predicted. $\alpha \gg 1$ signifies a substantial anisotropic hardening in domains with types (ii) and (iii) substructure, while χ significantly smaller than 1 indicates substantial reduction of the hardening rate in MSB domains.

The predicted lattice rotations, localization response, domain boundary orientation evolution and CRSS evolution in all three crystals are now described.

4.3 Lattice rotation

The evolution with strain of the lattice orientation, $\omega^{[l]}$, in individual domains, $l = 1, 2, \ldots, N = 16$ of the C, RC and G crystals is shown in Figs. 6(a), (b) and (c), respectively. It is seen from Fig. 6(a) that in the C crystal, for $\epsilon_{\mathrm{vM}} < 0.29$, the lattice orientations of all domains evolve similarly toward the D-orientation (Bunge angles: $(\phi_1, \varphi, \phi_2) = (-90^\circ, 27.22^\circ, 45^\circ)$). For $\epsilon_{\mathrm{vM}} \leq 0.29$, Eq. (35) is satisfied in all domains of the model crystal, as shown below. At $\epsilon_{\mathrm{vM}} = 0.29$ the domain boundaries of a certain domain become orientationally unstable. Following Sec. 3.5, this domain is therefore identified as an MSB. The lattice orientation of the MSB domain increasingly deviates from that of the other $N - 1 = 15$ domains with strain.

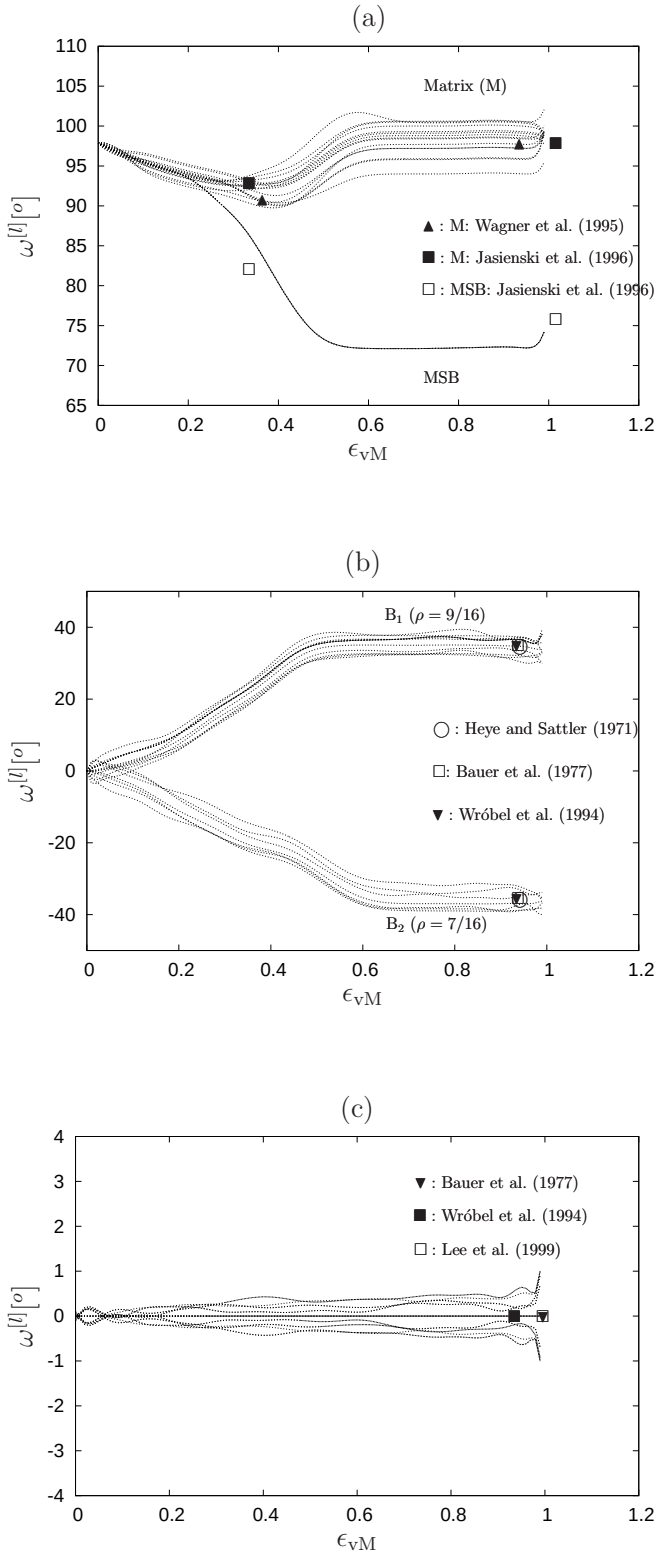

Fig. 6. Evolution with strain of the lattice orientation, ω, in the (a) C, (b) RC and (c) G crystals.

For $\epsilon_{\mathrm{vM}} \leq 0.29$, in all the domains of the C crystal, as noted in Sec. 4.1, two coplanar (b_2 and b_4) and two co-directional slip systems (a_6 and d_6) are activated. The co-directional slip systems a_6 and d_6 are simultaneously activated cross-slip systems, defined in Sec. 3.4 and therefore, their activities do not enter into the summation of Eq. (34). Identifying the crystallographic b-plane with p^* for which, $\dot{\Gamma}_{p^*} > 0$ and any of the other crystallographic planes with p^{**} for which, $\dot{\Gamma}_{p^{**}} = 0$, the ratio between two largest slip-rates, $\dot{\Gamma}_{p^*}/\dot{\Gamma}_{p^{**}} = \infty$, which implies the satisfaction of Eq. (35).

Fig. 6(b) shows the evolution of the lattice orientation in all domains of the model RC crystal. Starting already at $\epsilon_{\mathrm{vM}} = 0$, two orientationally unstable domain boundaries separate the model crystal into two sets of contiguous domains. One set of 7 domains rotate clockwise and the other set of 9 domains rotate counter-clockwise about TD. At $\epsilon_{\mathrm{vM}} = 0$, Eq. (35) is not satisfied in any of the model domains, as shown below. Following Sec. 3.5, therefore, these two sets of domains are identified as RDBs and denoted B_1 and B_2.

In the RC crystal, as noted in Sec. 4.1, two sets of coplanar slip systems (CP_1: b_2 and b_4, and CP_2: c_1 and c_3) are activated. If the crystallographic b-plane is identified with p^* and the crystallographic c-plane with p^{**}, $\dot{\Gamma}_{p^*}/\dot{\Gamma}_{p^{**}} \approx 1$, so that Eq. (35) for the dominance of a single crystallographic slip plane is not satisfied at the instant of banding.

Finally, Fig. 6(c) shows the lattice orientation evolution in all domains of the G crystal with deformation. It is clear that no domain is predicted to rotate significantly away from the initial Goss orientation. Thus, the G crystal is predicted to form neither MSBs or RDBs.

4.4 Slip accumulation

The total accumulated slip, $\Gamma^{[l]}$, in each of the $N = 16$ domains of the C, RC and G crystals is shown in Fig. 7. In the model C crystal it is seen from Fig. 7(a) that one domain, which was identified as an MSB in Sec. 4.3, accumulates one order of magnitude more slip compared to the other 15 domains, which were identified as the matrix band by $\epsilon_{\mathrm{vM}} = 1$. The latter set of domains are seen to undergo relatively little slip once macroscopic shear banding begins at $\epsilon_{\mathrm{vM}} = 0.29$, as evidenced by the nearly constant value of $\Gamma^{[l]}$ in Fig. 7(a) for $\epsilon_{\mathrm{vM}} > 0.29$. No such separation of domains on the basis of slip activity is observed in the case of the RC or G crystals in Figs. 7(b) and 7(c).

To quantify the concentration of slip in a single domain, a localization parameter, L, is defined as

$$L = \frac{\max_{1\leq l\leq N} \Gamma^{[l]}}{(\sum_{l=1}^{N} \Gamma^{[l]} - \max_{1\leq l\leq N} \Gamma^{[l]})/(N-1)}. \tag{44}$$

L is thus the ratio of the maximum accumulated slip in a domain to the average accumulated slip, where the average is calculated by excluding the contribution of the domain with the maximum accumulated slip. Fig. 8 shows that L in the macroscopic shear banding C crystal at $\epsilon_{\mathrm{vM}} = 1$ is one order of magnitude greater than that in either the regular deformation banding RC or homogeneously deforming G crystals. Intense shear localization in the C crystal occurs even though macroscopic shear banding was identified only in terms of lattice orientation deviation and pre-existing type (ii) substructure. Slip localization is thus orientation dependent.

The distribution of slip activity between the coplanar and co-directional slip systems in the domains of the C crystal is shown in Fig. 9. The slip accu-

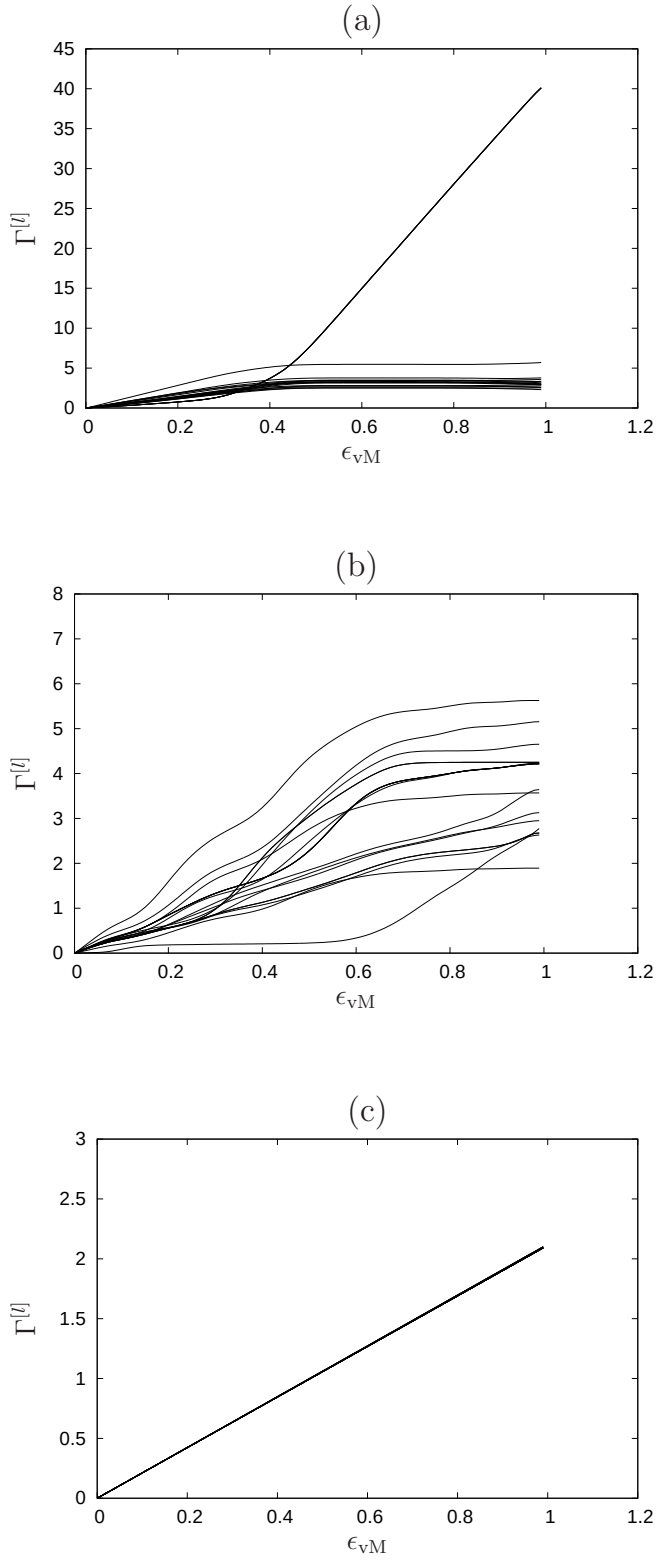

Fig. 7. Evolution with strain of the total accumulated slip $\Gamma^{[l]}$ in all the domains ($l = 1, 2, \ldots, N = 16$) of the (a) C, (b) RC and (c) G crystals.

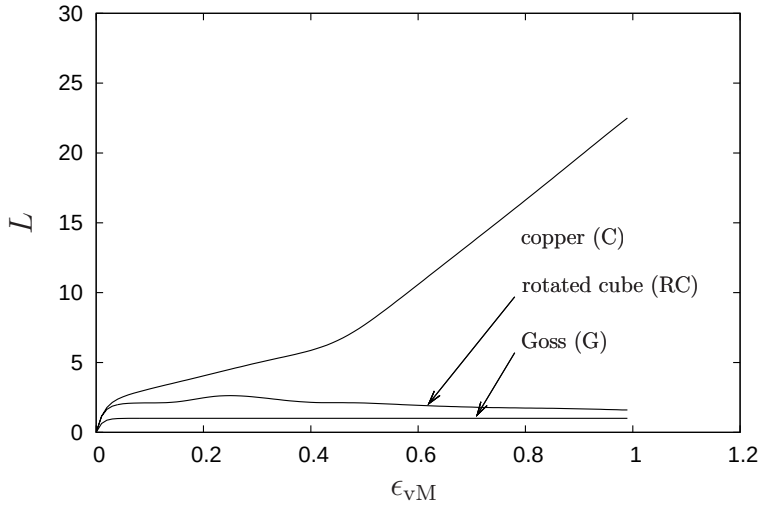

Fig. 8. Evolution with strain of localization parameter L, defined in Eq. (44), of the model C, RC and G crystals.

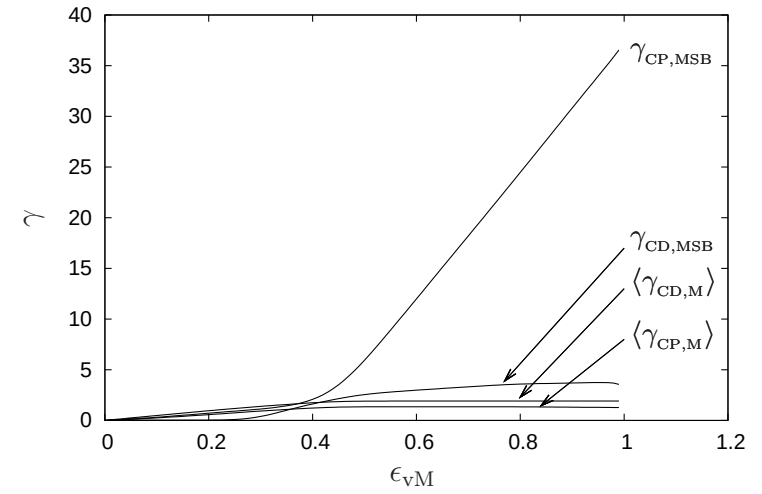

Fig. 9. Evolution with strain of slip (γ) in the individual slip systems of the MSB and the evolution with strain of slip averaged over the domains constituting the matrix band of the C crystal.

mulated in the coplanar and co-directional slip systems of the MSB domain are labeled $\gamma_{\mathrm{CP,MSB}}$ and $\gamma_{\mathrm{CD,MSB}}$, respectively. The coplanar and co-directional slip activity, averaged over the 15 domains comprising the matrix region are also shown, labeled as $\langle\gamma_{\mathrm{CP,M}}\rangle$ and $\langle\gamma_{\mathrm{CD,M}}\rangle$, respectively. It is noteworthy that the bulk of the deformation in the C crystal is accommodated by slip in the coplanar systems of the domain representing the MSB.

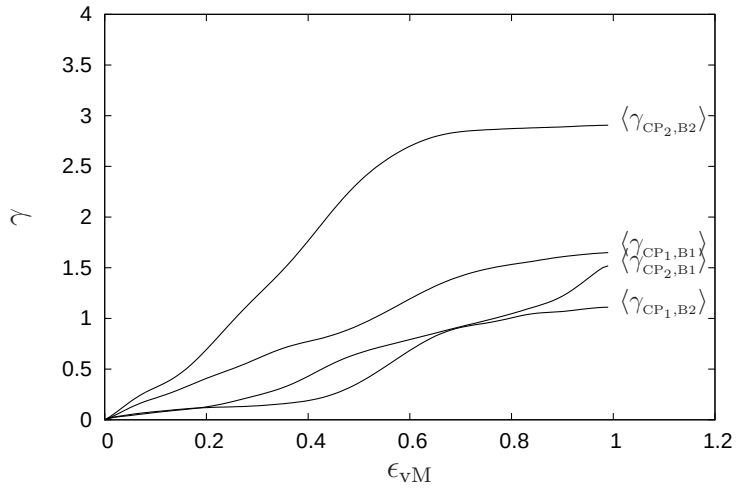

Fig. 10. Evolution with strain of the average accumulated slip (γ) in the two slip systems of bands B_1 and B_2 in the RC crystal.

The total slip averaged separately over the domains of RDBs B_1 and B_2 in the RC crystal is shown in Fig. 10. $\langle\gamma_{\mathrm{CP}_1,\mathrm{B}_1}\rangle$, $\langle\gamma_{\mathrm{CP}_2,\mathrm{B}_1}\rangle$, $\langle\gamma_{\mathrm{CP}_1,\mathrm{B}_2}\rangle$ and $\langle\gamma_{\mathrm{CP}_2,\mathrm{B}_2}\rangle$ represent the average accumulated slip of the two coplanar slip systems CP_1 and CP_2, in bands B_1 and B_2, respectively. In band B_1, CP_1 dominates CP_2, while in band B_2, CP_2 dominates CP_1. The quantitative condition for the dominance of one slip system in each of the two bands, Eq. (35), is satisfied for $\epsilon_{\mathrm{vM}} \geq 0.06$ in all the domains of both bands. Macroscopic shear banding may thus occur within the RDBs, as indeed observed by Wróbel et al. (1988). This secondary banding is not captured by the model.

4.5 Domain boundary orientation

The domain boundary orientation, θ, for the macroscopic shear banding C crystal evolves from about 15° to 45° following Eq. (39), as shown in Fig. 11(a). According to Eq. (39), the initial orientation of the domain boundaries in the RC crystal is $\theta = -3.75°$ and evolve with crystal shape (Sec. 3.6) into

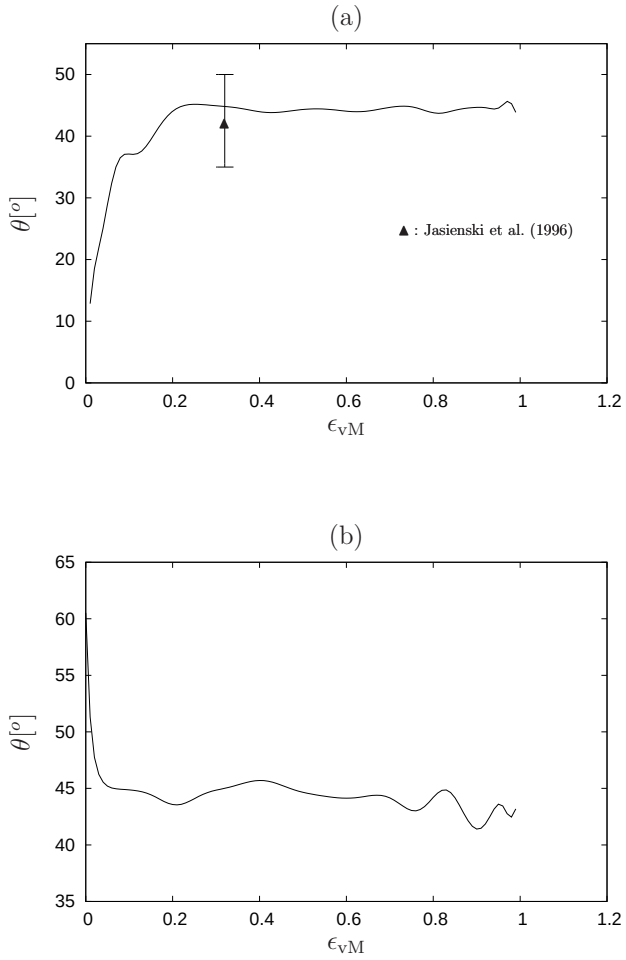

Fig. 11. Evolution with strain of the domain boundary orientation θ, defined in Fig. 5, in the (a) C and (b) G crystals.

alignment with the rolling plane. The predicted evolution of the very slightly misoriented domain boundaries in the G crystal is shown in Fig. 11 (b). As in the C crystal, these boundaries also align close to $\theta = 45^\circ$ eventually.

4.6 Evolution of the critical resolved shear stress

The evolution of the normalized CRSS, $\hat{\tau} = \tau/\tau_0$, of the CP and CD slip systems in all the domains of the model C crystal is shown in Fig. 12. It is seen that the CRSS in all the domains evolve similarly, following $[H^{(\mathrm{ii})}]$ of

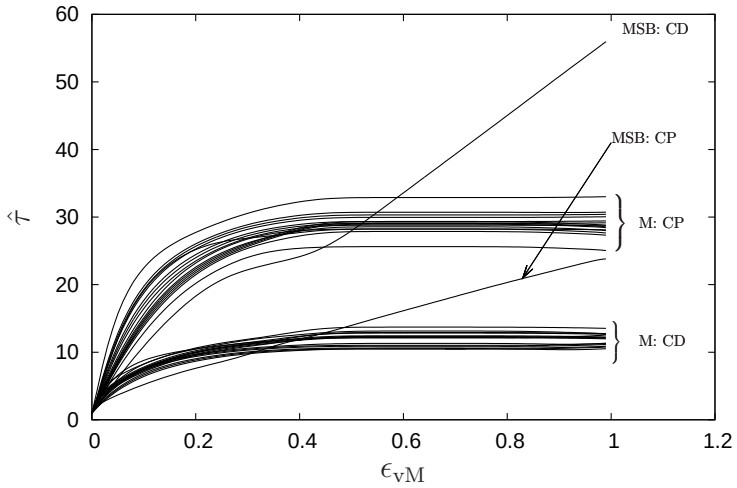

Fig. 12. Evolution with strain of the normalized critical resolved shear stress, $\hat{\tau} = \tau/\tau_0$, of the CP and CD slip systems in all the domains of the C crystal.

Eq. (43), until $\epsilon_{\mathrm{vM}} = 0.29$. At $\epsilon_{\mathrm{vM}} = 0.29$, as noted in Sec. 4.3, the MSB forms. Accordingly, further hardening of the MSB domain is governed by the latent hardening matrix, $[H^{(\mathrm{iii})}]$ of Eq. (43). This, together with the favorable orientation of the MSB, results in slip concentration in the CP system of the MSB, as seen in Fig. 9. This causes substantial latent hardening of the CD slip system in the MSB domain, as shown in Fig. 12. It is found that if $\chi > 0.5$ in Eq. (43), deformation localization does not occur.

RDBs form in the RC crystal already at $\epsilon_{\mathrm{vM}} = 0$, as noted in Sec. 4.3. At $\epsilon_{\mathrm{vM}} = 0$, Eq. (35) is not satisfied in the domains of either RDB, so that the hardening follows $[H^{(\mathrm{i})}]$ of Eq. (43). For $\epsilon_{\mathrm{vM}} \geq 0.06$, however, Eq. (35) is satisfied in all the domains of both RDBs and $[H^{(\mathrm{ii})}]$ represents the hardening matrix thereafter. In the G crystal, Eq. (35) is not satisfied throughout the deformation so that hardening follows $[H^{(\mathrm{i})}]$ of Eq. (43) throughout.

crystal	t_{stack} [s]	t_{Taylor} [s]	$t_{\text{domain}}/t_{\text{Taylor}}$
C	685	24	1.78
RC	423	21	1.26
G	435	22	1.24

Table 1

Simulation time, in seconds, of the C, RC and G crystals with $N = 16$ domains (t_{stack}) and $N = 1$ domain (Taylor model, t_{Taylor}). It is seen that $t_{\text{stack}} \sim N t_{\text{Taylor}}$.

4.7 Computational time

The wall clock computational time t_{stack}, in seconds, required to simulate plane strain deformation to $\epsilon_{\text{vM}} = 1$ of the C, RC and G crystals comprised of $N = 16$ domains is given in Tab. 1 . The time, in seconds, required for the corresponding Taylor model (Taylor, 1938), t_{Taylor}, is also given. The simulations are carried out in a standard 2.6GHz processor PC. It is seen from Tab. 1 that $t_{\text{stack}} = \beta N t_{\text{Taylor}}$, where $1 < \beta < 2$. The present calculations are thus only slightly slower than Taylor calculations and therefore, significantly faster than CPFEM simulations (Pierce et al., 1983; Anand and Kalidindi, 1993).

5 Discussion

5.1 C crystal

In agreement with experimental observations (Wagner et al., 1995; Jasienski et al., 1996) the model C crystal undergoes macroscopic shear banding. Model MSBs form only after considerable rolling reduction, as in the experiment of Wagner et al. (1995). Also in accord with experimental observations (Wag-

ner et al., 1995; Jasienski et al., 1996), model domains rotate toward the D-orientation prior to macroscopic shear banding. After banding, while the MSB domain rotates progressively toward the Goss orientation, the matrix domains rotate back toward the C orientation. Quantitative comparison of the present predictions with experimentally measured orientations (Wagner et al., 1995; Jasienski et al., 1996) is shown in Fig. 6(a) at three rolling reductions and agreement to within a few degrees is found. Finally, the predicted $\theta = 45^\circ$ inclination of the macroscopic shear band boundary, shown in Fig. 11(a), is close to the experimentally observed MSB inclination of 42° after 27% reduction in channel die compression, reported by Jasienski et al. (1996).

5.2 RC crystal

For the model RC crystal, quantitative agreement of the predicted lattice orientations of RDBs, B_1 and B_2, with the experimental measurements from the literature (Heye and Sattler, 1971; Bauer et al., 1977; Butler and Hu, 1989; Wróbel et al., 1994) at different strain-levels is shown in Fig. 6(b). In agreement with experimental observations (Heye and Sattler, 1971), localization is not observed and RDB formation occurs already at $\epsilon_{\mathrm{vM}} = 0$. The experimentally observed alignment of RDB boundaries with the rolling plane (Heye and Sattler, 1971) is also captured by the present model, as noted in Sec. 4.5.

5.3 G crystal

In the G crystal, in agreement with experimental observations (Bauer et al., 1977; Wróbel et al., 1994; Lee et al., 1999) to within a few degrees, no domain

is predicted to rotate significantly away from the initial Goss orientation, as shown in Fig. 6(c). The predicted domain boundaries in the G-crystal, which separate only slightly misoriented domains, represent neither MSB nor RDB boundaries. It may be supposed that they represent smaller scale dislocation boundaries such as DDW-MBs. However, the predicted boundary orientation is not in accord with this supposition. Because, while $\theta \approx 45^\circ$ boundaries are predicted in Fig. 11(b), it is experimentally observed (Ananthan et al., 1991) that DDW-MBs in Goss oriented grains in a copper polycrystal align with the active slip planes, which are inclined approximately 35° to RD. It is thus clear that the present approach is unsuccessful in predicting DDW-MB orientations.

6 Conclusions

A computationally efficient crystal plasticity model of a single crystal, based on the 'stack of domains' model of Arul Kumar et al. (2011) and capable of predicting experimentally observed regular deformation banding and macroscopic shear banding has been developed. Predicted macroscopic banding response, lattice orientation evolution, slip distribution and band boundary evolution during plane strain compression in three copper single crystals initially in the copper, rotated cube and Goss orientations compare well with experimental observations reported in the literature. The present model is unable to predict the alignment of smaller scale dislocation boundaries such as DDW-MBs, however.

Acknowledgments: We thank Prof. V. Parameswaran for encouragement and for comments that helped improve this manuscript. Funding was provided by the Indira Gandhi Center for Atomic Research, Kalpakkam.

References

Akef, A., Driver, J. H., 1991. Orientation splitting of cube-oriented face-centered cubic crystals in plane strain compression. Mater. Sci. Eng., A 132, 245–255.

Albou, A., Driver, J. H., Maurice, C., 2010. Microband evolution during large plastic strains of stable $\{110\}\langle 112\rangle$ Al and Al-Mn crystals. Acta mater 58, 3022–3034.

Anand, L., Aslan, O., Chester, S., 2012. A large-deformation gradient theory for elastic-plastic materials: strain softening and regularization of shear bands. Int. J. Plast.Doi: 10.1016/j.ijplas.2011.10.002.

Anand, L., Kalidindi, S. R., 1993. The process of shear band formation in plane strain compression of fcc metals: Effects of crystallographic texture. Mech. Mater. 17 (2–3), 223–243.

Anand, L., Kothari, M., 1996. A computational procedure for rate-independent crystal plasticity. J. Mech. Phys. Solids 44 (4), 525–558.

Ananthan, V. S., Leffers, T., Hansen, N., 1991. Characteristics of 2nd generation microbands in cold-rolled copper. Scr. Metall. Mater. 25, 137–142.

Arul Kumar, M., Mahesh, S., Parameswaran, V., 2011. A stack model of rate-independent polycrystals. Int. J. Plast. 27 (6), 962–981.

Asaro, R. J., 1979. Geometrical effects in the inhomogeneous deformation of ductile single crystals. Acta Metall. 27 (3), 445–453.

Barrett, C. S., 1939. Structure of iron after compression. Trans. AIME 135, 296–352.

Barrett, C. S., Levenson, L. H., 1940. Structure of aluminum after compression. Trans. AIME 137, 112–127.

Bauer, R. E., Mecking, H., Lucke, K., 1977. Textures of copper single crystals

after rolling at room temperature. Mater. Sci. Eng. 27 (2), 163–180.

Bay, B., Hansen, N., Kuhlmann-Wilsdorf, D., 1989. Deformation structures in lightly rolled pure aluminum. Mater. Sci. Eng. A 113, 385–397.

Biot, M. A., 1965. Mechanics of Incremental Deformations. John Wiley and Sons, New York, London.

Bishop, J. F. W., Hill, R., 1951. A theory of the plastic distortion of a polycrystalline aggregate under combined stresses. Philos. Mag. 42 (327), 414–427.

Blicharski, M., Dymek, S., Wróbel, M., 1995. J. mater. proc. tech. Inhomogeneities of microstructure evolved in metals under plastic deformation 53, 75–84.

Butler, J. F., Hu, H., 1989. Channel die compression of aluminum single crystals. Mater. Sci. Eng., A 114, L29–L33.

Cahn, R. W., 1951. Slip and polygonization in aluminium. J. Inst. Metals 79, 129–158.

Chang, Y.-C., 2009. N dimension golden section search: its variants and limitations. In: Shi, R., Fu, W., Wang, Y., Wang, H. (Eds.), Proc. 2nd Int. Conf. Biomedical Engineering and Informatics. IEEE, p. 5304779.

Chin, G. Y., 1971. The inhomogeneity of plastic deformation. ASM, Metals park, Ohio.

Chin, G. Y., Hosford, W. F., Mendorf, D. R., 1969. Accommodation of constrained deformation in fcc metals by slip and twinning. Proc. R. Soc. London, Ser. A 309, 433–456.

Chin, G. Y., Mammel, W. L., 1969. Generalization and equivalence of the minimum work (Taylor) and maximum work (Bishop-Hill) principles of crystal plasticity. Trans. AIME 245, 1211.

Chin, G. Y., Wonsiewicz, B. C., 1969. Deformation banding and the stability $\langle 100\rangle$–$\langle 111\rangle$ fiber textures in FCC materials. Trans. AIME 245, 871–872.

Cizek, P., Parker, B. A., Wynne, B. J., 1995. Dense dislocation walls and deformation banding in commercial purity aluminum. Scr. Metall. 32 (3), 319–323.

Dillamore, I. L., Roberts, J. G., Bush, A. C., 1979. Occurrence of shear bands in heavily rolled cubic metals. Metal Science 13, 73–77.

Duggan, B. J., Hatherly, M., Hutchinson, W. B., Wakefield, P. T., 1978. Deformation structures and textures in cold-rolled 70:30 brass. Metal Science 12, 343–350.

Gil Sevillano, J., Houtte, P. V., Aernoudt, E., 1980. Geometical models for polycrystal deformation and texture prediction. Prog. Mater. Sci. 25 (2-4), 71–412.

Groh, S., Marin, E. B., Horstemeyer, M. F., Zbib, H. M., 2009. Multiscale modeling of the plasticity in an aluminum single crystal. Int. J. Plast. 25 (8), 1456–1473.

Gurtin, M. E., 1981. An introduction to continuum mechanics. Academic Press, New York.

Hansen, N., Juul Jensen, D., 1999. Development of microstructrure in FCC metals during cold work. Phil Trans. R. Soc. Lond. A 357, 1447–1469.

Hatherly, M., Malin, A. S., 1984. Shear bands in deformed metals. Scr. Metall. 18, 449–454.

Havner, K. S., 1992. Finite Plastic Deformation of Crystalline Solids. Cambridge University Press.

Heye, W., Sattler, H. P., 1971. Bildung von deformationsbandern in gewaltzen kuper-einkristallen. Z. Metallkd. 62, 386–391.

Hill, R., 1961. Discontinuity relations in mechanics of solids. In: Sneddon, I. N., Hill, R. (Eds.), Prog. Solid Mech. Vol. 2. Interscience Publishers, New York, Ch. 6, pp. 247–278.

Hill, R., 1966. Generalized constitutive relations for incremental deformation of metal crystals by multislip. J. Mech. Phys. Solids 14 (2), 95–102.

Hill, R., Hutchinson, J. W., 1975. Bifurcation phenomena in the plane tension test. J. Mech. Phys. Solids 23 (4-5), 239–264.

Huang, C. X., Wang, K., Wu, S. D., Zhang, Z. F., Li, G. Y., Li, S. X., 2006. Deformation twinning in polycrystalline copper at room temperature and low strain rate. Acta mater. 54 (3), 655–665.

Hughes, D. A., Chrzan, D. C., Liu, Q., Hansen, N., 1998. Scaling of Misorientation Angle Distributions. Phys. Rev. Lett. 81 (21), 4664–4667.

Hughes, D. A., Hansen, N., 1993. Microstructural evolution in nickel during rolling from intermediate to large strains. Metall. Mater. Trans. A 24 (9), 2021–2037.

Hughes, D. A., Liu, Q., Chrzan, D. C., Hansen, N., 1997. Scaling of microstructural parameters: Misorientations of deformation induced boundaries. Acta Mater. 45 (1), 105–112.

Jasienski, Z., Baudin, T., Piatkowski, A., Penelle, R., 1996. Orientation changes inside shear bands occurring in channel-die compressed (112)[$\bar{1}\bar{1}$1] copper single crystals. Scr. Mater. 35 (3), 297–403.

Kanjarla, A. K., Van Houtte, P., Delannay, L., 2010. Assessment of plastic heterogeneity in grain interaction models using crystal plasticity finite element method. Int. J. Plast. 26, 1220–1233.

Kocks, U. F., Tomé, C. N., Wenk, H. R., 1998. Texture and anisotropy. Cambridge Univ. Press, Cambridge, U.K.

Korbel, A., Szczerba, M., 1982. Strain hardening of copper single crystals at high strains and dynamical recovery process. Acta metall., 1961–1968.

Kratochvíl, J., Kružík, M., Sedláček, R., 2007. Statistically based continuum model of misoriented dislocation cell structure formation. Phys. Rev. B 75,

064104.

Kuhlmann-Wilsdorf, D., 1999. Regular deformation bands (DBs) and the LEDS hypothesis. Acta Mater. 47 (6), 1697–1712.

Kulkarni, S. S., Starke Jr, E. A., Kuhlmann-Wilsdorf, D., 1998. Some observations on deformation banding and correlated microstructures of two aluminum alloys compressed at different temperatures and strain rates. Acta Mater. 46 (15), 5283–5301.

Kuroda, M., Tvergaard, V., 2007. Effects of texture on shear band formation in plane strain tension/compression and bending. International Journal of Plasticity 23 (2), 244 – 272.

Lebensohn, R. E., Tomé, C. N., 1993. A self-consistent anisotropic approach for the simulation of plastic deformation and texture development of polycrystals: application to zirconium alloys. Acta Metall. Mater. 41 (9), 2611–2624.

Lee, C. S., Duggan, B. J., 1993. Deformation banding and copper-type rolling textures. Acta Metall. Mater. 41 (9), 2691–2699.

Lee, C. S., Duggan, B. J., Smallman, R. E., 1993. A theory of deformation banding in cold rolling. Acta Metall. Mater. 41 (8), 2265–2270.

Lee, K. C., Zeng, Y. P., Lee, C. S., 1999. Influence of external constraint on deformation banding of $\{110\}\langle uvw\rangle$ orientations. Scr. Mater. 40 (2), 197–202.

Leffers, T., 2001a. A model for rolling deformation with grain subdivision. part I: The initial stage. Int. J. Plast. 17 (4), 469–489.

Leffers, T., 2001b. A model for rolling deformation with grain subdivision. part II: The subsequent stage. Int. J. Plast. 17 (4), 491–511.

Liu, Q., Hansen, N., 1998. Macroscopic and microscopic subdivision of a cold-rolled aluminium single crystal of cubic orientation. Proc. R. Soc. London, Ser. A 454, 2555–2592.

Liu, Q., Jensen, D. J., Hansen, N., 1998. Effect of grain orientation on deformation structure in cold rolled polycrystalline aluminium. Acta Mater. 46 (16), 5819–5838.

Mahesh, S., 2006. Deformation banding and shear banding in single crystals. Acta Mater. 54 (17), 4565–4574.

Mahesh, S., 2009. A hierarchical model for rate-dependent polycrystals. Int. J. Plast. 25 (5), 752–767.

Mahesh, S., 2010. A binary tree based model for rate-independent polycrystals. Int. J. Plast. 26 (1), 42–64.

Mahesh, S., Tomé, C. N., 2004. Deformation banding under arbitrary monotonic loading in cubic metals. Philos. Mag. 84, 3517–3546.

Morii, K., Nakayama, Y., 1981. Shear bands in rolled copper single crystals. Trans. JIM 22 (12), 857–864.

Nakayama, Y., Morii, K., 1982. Transmission electron microscopy of shear band formation in rolled copper single crystal. Trans. JIM 23 (7), 422–431.

Needleman, A., Rice, J. R., 1978. Limits to ductility set by plastic flow localization. In: Koistinen, D. P., Wang, N. M. (Eds.), Mechanics of Sheet Metal Forming. Plenum Publication Corp., pp. 237–267.

Nye, J. F., 1953. Some geometrical relations in dislocated crystals. Acta Metall. 1, 153–162.

Ortiz, M., Repetto, E. A., 1999. Nonconvex energy minimization and dislocation structures in ductile single crystals. J. Mech. Phys. Solids 47, 397–462.

Ortiz, M., Repetto, E. A., Stainier, L., 2000. A theory of subgrain dislocation structures. J. Mech. Phys. Solids 48, 2077–2114.

Paul, H., Maurice, C., Driver, J. H., 2010. Microstructure and microtexture evolution during strain path changes of an initially stable Cu single crystal. Acta mater. 58 (8), 2799–2813.

Pierce, D., Asaro, R. J., Needleman, A., 1982. An analysis of nonuniform and localized deformation in ductile single crystals. Acta Mater. 30, 1087–1119.

Pierce, D., Asaro, R. J., Needleman, A., 1983. Material rate dependence and localized deformation in crystalline solids. Acta Metall. 31 (12), 1951–1976.

Raabe, D., Zhao, Z., Roters, F., 2004. Study on the orientational stability of cube-oriented fcc crystals under plane strain by use of a texture component crystal plasticity finite element method. Scr. Mater. 50 (7), 1085–1090.

Rezvanian, O., Zikry, M. A., Rajendran, A. M., 2006. Microstructural modeling of grain subdivision and large strain inhomogeneous deformation modes in f.c.c. crystalline materials. Mech. Mater. 38 (12), 1159–1169.

Si, L. Y., Lu, C., Huynh, N. N., Tieu, A. K., Liu, X. H., 2008. Simulation of rolling behaviour of cubic oriented al single crystal with crystal plasticity FEM. J. Mater. Process. Technol. 201 (1–3), 79–84.

Taylor, G. I., 1938. Plastic strain in metals. J. Inst. Metals 62, 307.

Tomé, C., Canova, G. R., Kocks, U. F., Christodoulou, N., Jonas, J. J., 1984. The relation between macroscopic and microscopic strain hardening in F.C.C polycrystals. Acta Metall. 32 (10), 1637–1653.

Van Houtte, P., Delannay, L., Samajdar, I., 1999. Quantitative predictions of the cold-rolling texture in low-carbon steel by means of the LAMEL model. Textures and Microstructures 31 (3), 104–119.

Van Houtte, P., Sevillano, J. G., Aernoudt, E., 1979. Models for shear band formation in rolling and extrusion. Z. Metallkd. 70, 426–432.

Wagner, P., Engler, O., Lücke, K., 1995. Formation of Cu-type shear bands and their influence on deformation and texture of rolled FCC $\{112\}\langle 111\rangle$ single crystals. Acta Metall. Mater. 43 (10), 3799–3812.

Wert, J. A., Kashihara, K., Okada, T., Huang, X., Inoko, F., 2005. Deformation band evolution in [110] al single crystals strained in tension. Philos.

Mag. 85 (18), 1989–2006.

Winther, G., Juul Jensen, D., Hansen, N., 1997. Dense dislocation walls and microbands aligned with slip planes – Theoretical considerations. Acta Mater. 45 (12), 5059–5068.

Wróbel, M., Dymek, S., Blicharski, M., 1996. The effect of strain path on microstructure and texture development in copper single crystals with (110)[001] and (110)[1$\bar{1}$0] initial orientations. Scripta mater. 35 (3), 417–422.

Wróbel, M., Dymek, S., Blicharski, M., Gorczyca, S., 1988. The development of dislocation structure and texture in rolled copper (001)[110] single crystals. Textures and Microstructures 10 (1), 67–75.

Wróbel, M., Dymek, S., Blicharski, M., Gorczyca, S., 1994. Dislocation microstructure and texture development in rolled copper single crystals. Z. Metallkd. 85 (6), 415–425.

Zhang, F., Bower, A. F., Mishra, R. K., Boyle, K. P., 2009. Numerical simulations of necking during tensile deformation of aluminum single crystals. Int. J. Plast. 25 (1), 49–69.